Direct numerical simulation of cylindrical particle-laden gravity currents

Nadim Zgheib, Thomas Bonometti, Sivaramakrishnan Balachandar

Direct numerical simulation of cylindrical particle-laden gravity currents

N. Zgheib [a,b], T. Bonometti [b,c], S. Balachandar [a,*]

[a] Department of Mechanical and Aerospace Engineering, University of Florida, Gainesville, FL 32611,USA
[b] Université de Toulouse, INPT, UPS, IMFT (Institut de Mécanique des Fluides de Toulouse), UMR 5502, Allée Camille Soula, F-31400 Toulouse, France
[c] CNRS; IMFT; F-31400 Toulouse, France

Keywords:
Direct numerical simulations
Particle-laden flow
Turbidity currents

A B S T R A C T

We present results from direct numerical simulations (DNS) of cylindrical particle-laden gravity currents. We consider the case of a full depth release with monodisperse particles at a dilute concentration where particle–particle interactions may be neglected. The disperse phase is treated as a continuum and a two-fluid formulation is adopted. We present results from two simulations at Reynolds numbers of 3450 and 10,000. Our results are in good agreement with previously reported experiments and theoretical models. At early times in the simulations, we observe a set of rolled up vortices that advance at varying speeds. These Kelvin–Helmholtz (K–H) vortex tubes are generated at the surface and exhibit a counter-clockwise rotation. In addition to the K–H vortices, another set of clockwise rotating vortex tubes initiate at the bottom surface and play a major role in the near wall dynamics. These vortex structures have a strong influence on wall shear-stress and deposition pattern. Their relations are explored as well.

1. Introduction

Particle driven currents are a special form of gravity currents in which the density difference is caused by the suspension of particles within an interstitial fluid forming the current. If the mixture density of such a suspension is larger than that of the ambient fluid, it will advance primarily horizontally as a turbidity current [12,17]. Turbidity currents are inherently more complex than homogeneous conservative currents because the density of the current (and consequently the density difference between the current and the ambient) may vary temporally and spatially as a result of the settling and entrainment of particles. The effective settling speed of particles, for example, may depend on particle Reynolds number, particle flocculation, and interaction with surrounding turbulence. On the other hand, if the current is traveling fast enough over an erodible bed, it may entrain particles causing it to move even faster and consequently entrain more particles in a self-reinforcing cycle.

Particulate gravity currents are observed in many industrial, environmental, and geological situations. Owing to their destructive nature, turbidity currents constitute a major factor in the design of underwater structures such as pipelines and cables [22]. In an industrial context, they are essential for transporting sediments that may contain pollutants. Furthermore, they are responsible for the formation of submarine canyons as well as for sedimentation transport into the deep oceans.

Particulate constant volume releases [1–3,6,12,14,18] have been studied. However, these finite releases are invariably dominated by fronts. Often in turbidity currents, it is very important to look at the body of the current after the head had long moved away. Experimental and computational investigation of the body is somehow harder and is usually investigated through constant flux currents [11,16,20,23]. In the present context, we explore a finite-volume cylindrical release of particle-laden fluid in clear ambient surrounding. We wish to identify the dynamics of the current, specifically the three-dimensional propagation and vortical structures of the current. Here we are only concerned with deposition and neglect the effects of resuspension. In reality, resuspension of particles may play a role, but the mechanisms of re-suspension are not fully understood and models of resuspension rate remain empirical with large uncertainties (see [26]). In order to make the problem simple and manageable, we look only at the problem of deposition.

Predicting the deposition pattern or the sediment erosion resulting from a turbidity current necessitates a good understanding of the mechanism of sediment transport and particle deposition, which are highly dependent on the dynamics of the current, the level of turbulence, and the fluid-particle interaction. As a result, a great level of simplification is generally taken, usually through depth averaging, when studying particulate-driven currents. Some of the models include the Box Model [2,9], which is a simple and fast way to model the extent, speed, and sedimentation rate of turbidity currents. The Box Model is not directly derived from the Navier–Stokes equations; however, it considers the current to evolve with negligible entrainment through a series of height diminishing concentric cylinders for an axisymmetric lock release configuration. In addition to depth averaging, no radial variation is allowed.

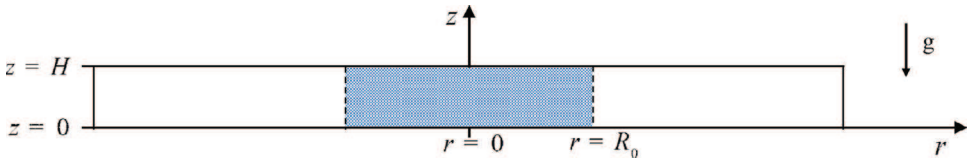

Fig. 1. Side view of the initial setup of the cylindrical lock-exchange flow inside a rectangular box of size $L_x \times L_y \times H = 30 \times 30 \times 1$. Initially, a cylindrical gate of radius $R_0 = 2$ placed at the center of the domain separates particle-laden fluid from the ambient clear fluid. Once the gate is lifted, the simulation starts and the particle-laden fluid begins to intrude horizontally into the ambient.

A more complex model is based on the Shallow Water equations [3,24,8], which are derived by vertically averaging the Navier–Stokes equations under the assumption of high length-to-thickness aspect ratio. However, because of the variable volume fraction of the current, an equation of particle conservation is further required. Such models do not usually account for sediment entrainment on the basis that the velocities are insufficient to lift up particles, however the flow is considered to be sufficiently energetic so that turbulent mixing maintains vertically uniform properties.

Most research on axisymmetric particle-laden gravity currents has mainly revolved around the early experiments of Bonnecaze et al. [3] and theoretical models mostly based on the Box Model and Shallow Water equations [24,13]. Our objective in this study is to consider a scenario that is similar to what has been investigated experimentally and examine it through direct numerical simulations. Highly resolved simulations for cylindrical density-driven finite-release currents have been investigated in the past with results comparing favorably with experiments [4]. Here we consider direct numerical simulations of particle-laden currents resulting from the release of an initial cylindrical fluid-particle mixture.

The DNS will allow us to explore the three-dimensional structures of the current from iso-surfaces of density and iso-surfaces of the swirling strength that show the intensity and structure of the coherent eddies. In many applications, these large scale vortical structures will play an important role in the erosion and resuspension of particles by locally modifying the shear stress at the bottom wall. They also play an important role in the deposition of particles by transporting low particle concentration fluid (particle-laden current mixed with ambient) from the current's top layers towards the bottom wall and consequently decreasing the local settling rate. This study will be limited to finite-releases of full-depth cylindrical gravity currents with dilute concentrations of monodisperse particles. The paper is arranged as follows. The mathematical formulation is outlined Section 2. In Section 3, we present our simulation results and compare, where possible, to previous experimental and theoretical data. Finally, main conclusions are presented in Section 4.

2. Mathematical formulation

A side view of the problem setup is shown in Fig. 1. Initially, a cylindrical gate separates a relatively heavier (compared with the ambient) particle-laden fluid of initial density $\rho_{c0} = (\rho_p - \rho_a)\phi_0 + \rho_a$ in its interior from the surrounding clear ambient fluid of density ρ_a. Both fluids are initially at the same level and occupy the entire height of the domain (see Fig. 1). Here, ρ_p represents the density of suspended particles, and ϕ_0 is the initial volume fraction occupied by those particles.

Our focus is to simulate buoyancy driven flows with dilute suspensions, where particle-particle interactions may be neglected. We consider monodisperse particles whose size is much smaller than characteristic length scale H of the problem. The particle-laden solution will be treated as a continuum and a two-fluid formulation is adopted. We follow Cantero et al. [6] by implementing an Eulerian–Eulerian model of the two-phase flow equations. The model involves (i) mass (ii) and momentum conservation equations for the continuum fluid phase, (iii) an algebraic equation for the particle phase where the particle velocity is taken to be equal to the local fluid velocity and an imposed settling velocity derived from the Stokes drag force on the particles, (iv) and a transport equation for the volume fraction (particle phase). The non-dimensional system of equations read

$$\nabla \cdot \mathbf{u} = 0 \tag{1}$$

$$\frac{D\mathbf{u}}{Dt} = \phi \mathbf{e}^g - \nabla p + \frac{1}{Re}\nabla^2 \mathbf{u} \tag{2}$$

$$\mathbf{u}_p = \mathbf{u} + \mathbf{u}_s \tag{3}$$

$$\frac{\partial \phi}{\partial t} + \nabla \cdot (\phi \mathbf{u}_p) = \frac{1}{Sc\,Re}\nabla^2 \phi \tag{4}$$

Here $\mathbf{e}^g$ is a unit vector pointing in the direction of gravity. Unless otherwise stated, all parameters are non-dimensionalized. The height H of the domain is taken as the length scale, $U = \sqrt{g'_0 H}$ as the velocity scale, $T = H/U$ as the time scale, ρ_a as the density scale, and $\rho_a U^2$ as the pressure scale. The reduced gravitational acceleration is defined as $g'_0 = (\rho_p - \rho_a)\phi_0 g/\rho_a$. We denote by $\mathbf{u}_p$ and ϕ the velocity and the volume fraction of the particle phase, respectively. $\mathbf{u}$ and p correspond to the velocity and total pressure of the continuum fluid phase, respectively. The settling velocity $\mathbf{u}_s$ is determined from the Stokes drag force on spherical particles with small particle Reynolds numbers. Here, the density of particles is assumed to be appreciably larger than that of the ambient fluid such that the dominant force on the particle is the Stokes drag. The Reynolds and Schmidt numbers in Eqs. (2) and (4) are defined as

$$Re = UH/\nu, \quad Sc = \nu/\kappa \tag{5}$$

In the above, κ and ν represent the molecular diffusivity and kinematic viscosity of the ambient (interstitial) fluid, respectively.

The simulation is carried out inside a rectangular box of dimensions $L_x \times L_y \times H = 30 \times 30 \times 1$ using a spectral code that has been extensively validated [4,5]. Periodic boundary conditions are imposed along the sidewalls for the continuous and particle phases. No-slip and free-slip conditions are imposed for the continuous phase along the bottom and top walls, respectively. Mixed and Neumann boundary conditions are imposed for the particle phase at the top and bottom walls, which translate into zero particle net flux and zero particle resuspension, respectively.

$$\boxed{\text{at } z = 1 \quad \frac{1}{Sc\,Re}\frac{\partial \phi}{\partial z} - \mathbf{u}_s \phi = 0,} \qquad \boxed{\text{at } z = 0 \quad \frac{\partial \phi}{\partial z} = 0.} \tag{6}$$

To be more explicit, the condition (6) at the bottom wall allows for a non-zero advective flux which is due to the sedimentation of particles. Since we assume zero resuspension, the sediment flux across the bottom boundary is the deposit. For more details and a discussion about the choice of the present boundary conditions, the reader is referred to Cantero et al. [6]. We present results from two simulations that differ solely by the Reynolds number. The details

Table 1
Details from the numerical simulations performed for this study. *Re*, *Sc*, u_s, and ϕ_0 are the Reynolds, Schmidt, settling velocity, and initial volume fraction defined in Section 2. The simulations ran for t_f non-dimensional time units.

Domain size	*Re*	*Sc*	$\mathbf{u}_s$	ϕ_0	Grid resolution	Time step	t_f
$30 \times 30 \times 1$	10,000	1	0.013	$\ll 1$	$680 \times 680 \times 109$	2×10^{-3}	30
$30 \times 30 \times 1$	3450	1	0.013	$\ll 1$	$680 \times 680 \times 109$	2×10^{-3}	30

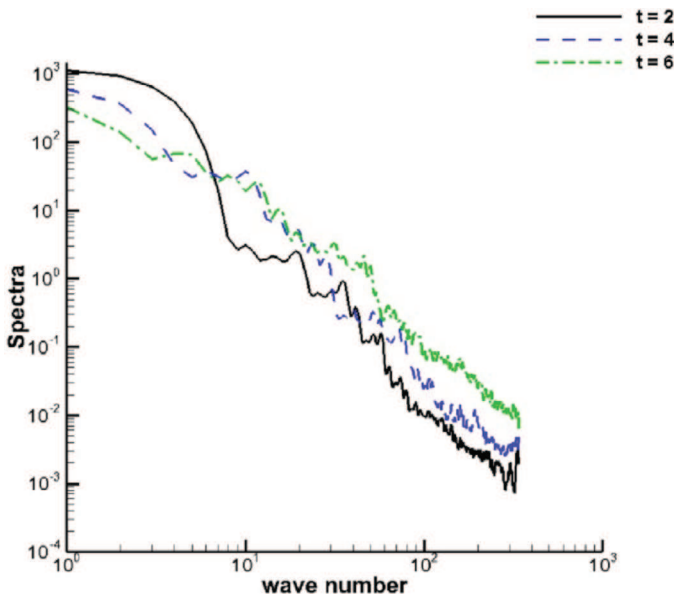

Fig. 2. Particle volume fraction spectra as a function of wavenumber along the *x*-direction for three different time instances at $Re = 10000$.

of the simulations are outlined in Table 1. The domain size was chosen for comparison purposes to correspond with the previous experiments of Bonnecaze et al. [3]. We chose a grid resolution of $680 \times 680 \times 109$ (along the *x*, *y*, and *z* directions, respectively) corresponding to over 50 million degrees of freedom. This numerical resolution, for the larger *Re* number case of 10,000, achieves between 4 and 6 decades of decay in the *x*-spectra of particle-volume fraction at various instances as shown in Fig. 2. Similar decay was observed for all other quantities and for the *y*-spectra and *z*-spectra as well. Thus, the simulations to be discussed here are well resolved.

3. Results

3.1. Three-dimensional structures

The start of the simulation is initiated by "lifting" the cylindrical gate. The particle-laden solution is heavy and begins to collapse and spread out radially, intruding into the ambient fluid with a slug-like ground hugging motion. In Fig. 3, we present iso-surfaces of concentration from the large *Re* number simulation of 10,000 to help visualize the three-dimensional temporal and spatial structures of the current as well as bottom iso-contours of concentration showing the lobe and cleft structures at the front. Shortly after release ($t = 2$), the front is nearly two-dimensional and the "head" of the current may be recognized by a rolled up vortex tube at the front. At later times ($t = 4$ and $t = 6$), a pattern of rolled up vortices can be identified. Because of their unequal propagation speeds, some of the relatively faster vortex tubes will catch up with slower tubes ahead and merge to form bigger rolled up vortices (see Fig. 3 at $t = 4$ and $t = 6$) Furthermore, as the current starts to decelerate, (and because of the no-slip boundary condition at the bottom surface) lobe and cleft structures [21, 15] begin to emerge rendering the once smooth front more complex and three-dimensional. The speed of the current continuously develops along its circumference, and as a result, the lobe and cleft structures evolve by merging and splitting along the front. In Fig. 3d, the current's front at three time instances is identified by the bottom iso-contour of $\phi = 0.05$. There we observe the lobes and clefts to grow in size from $t = 2$ to $t = 4$,and then maintain roughly the same size at $t = 6$. At $t = 4$, we may roughly estimate the number of these lobes and clefts where we observe the presence of 23 lobes (or clefts) in the chosen portion of the domain ($x \geq 1.5$, $y \geq 1.5$) This translates to approximately 200 lobes (or clefts) along the entire front. The thin dashed lines in Fig. 3d mark the locations of the clefts. Computing the mean front perimeter at $t = 4$, one may estimate the characteristic wavelength of the lobes and clefts to be roughly 1/10 the initial height of the current. This is in reasonable agreement with the characteristic size of lobes and clefts predicted by the linear stability analysis of Hartel et al. [15] in the case of a planar gravity current, for which the predicted wavelength is in the range 0.03–0.1 for Grashoff numbers between 5×10^6 and 5×10^8 (the Grashoff number of the present simulation is 10^7).

The primary vortical structures identified in Fig. 3 ($T_1 - T_4$) are the Kelvin-Helmholtz vortices generated at the current–ambient interface. These vortices exhibit a counter-clockwise rotation (in this paper, the direction of rotation of a vortex tube (clockwise or counter-clockwise) is taken to be that seen on the *x*-*z* plane viewed in the positive *y*-direction) and are advected radially outwards by the current. These energetic vortices locally accelerate the flow in the near wall region, and because of the no-slip boundary condition, help to initiate clockwise-rotating vortices at the bottom surface. The flow, in the near wall region, accelerates as it passes between the counter-clockwise rotating vortex and the bottom wall, and its dynamic pressure locally decreases. The flow then decelerates, as it passes beyond the radial location of the toroidal vortex tube, and is subjected to an adverse pressure gradient, which results in flow separation and the initiation of a clockwise-rotating bottom vortex($B_1 - B_3$) in Fig. 4d. These bottom vortices are concealed in the iso-surface plots, but may be readily visualized through iso-surface plots of the swirling strength λ_{ci} shown in Fig. 4. The swirling strength is a good indicator of regions of intense vortex structures [28,7]. It is defined as the absolute value of the imaginary portion of the complex eigenvalue of the velocity gradient tensor. At $t = 4$, the domain consists of four well-defined primary vortex tubes (T_{1-4}) that span the head and body of the current. In addition to these tubes, the bottom vortex ring B_1 starts to form just behind the head, where a set of closely packed, inclined hairpin vortices emerge from the surface denoting the elevated head of the current. At $t = 6$, two additional bottom vortex tubes have appeared (B_2 and B_3) and the overall vortical structures have become more complex. In the body of the current, inclined hairpin vortices have formed around the vortex tube B_2 (see inset).

The typical dimensional turnover time $\tau = T/(\lambda_{ci})_{\max}$ of the large scale vortical structures may be inferred from the maximum value of λ_{ci} (located at the center of each vortex) for each of these toroidal vortices. Moreover, by comparing the ratio of the dimensional Stokes time of the particles ($\tau_s = u_s/g$)to the dimensional typical turnover time $\tau$of the large scale vortical structures, we may verify, and assess (a posteriori) the validity of our numerical model, specifically that the particle velocity $\mathbf{u}_p$ defined in (3) may be directly obtained as the sum of the fluid velocity $\mathbf{u}$ and the settling velocity $\mathbf{u}_s$. The maximum value of the ratio of $\xi = \tau_s/\tau$was computed as a function of time and was always found to be less than 1%. This confirms that the present model, (i.e. Eq. 3), is appropriate in the present case.

3.2. One-dimensional time evolution

In Fig. 5, we plot the temporal evolution of the mean height $\bar{h}$ and areal deposit $\bar{D}$ of the current along the radial direction. These quantities are obtained by averaging along the azimuthal and vertical

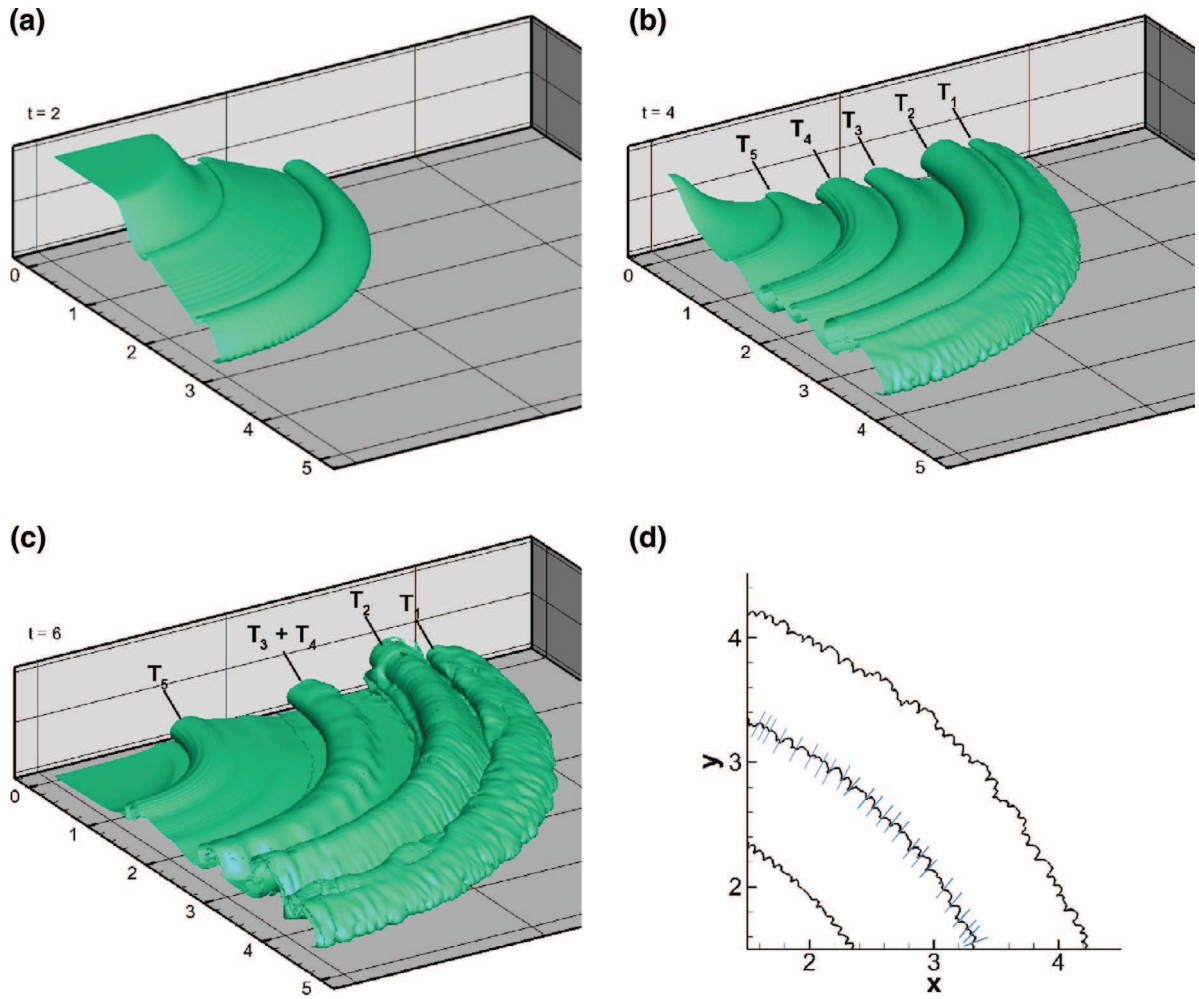

Fig. 3. (a)->(c) Iso-surfaces of concentration in first quadrant ($x \geq 0, y \geq 0$) of the computational domain for $Re = 10000$. The structure of the current exhibits multiple rolled-vortices with the lobe and cleft instability pattern identifiable at later times($t = 6$). An isovalue of $\phi = 0.25$ is employed for all cases. (d) Iso-contours of $\phi = 0.05$ at the bottom wall for $t = 2, 4, 6$ .Multiple lobe and cleft structures may be identified. Blue lines are added on the contour at $t = 4$ to show the characteristic size of these structures.

directions for the concentration field to calculate $\bar{h}$, and integrating in time the tangentially-averaged bottom concentration section (multiplied by the settling velocity) to obtain $\bar{D}$

$$\bar{h}(r,t) = \frac{1}{2\pi}\int_0^H \int_0^{2\pi} \phi(r,\theta,z,t)\,\mathrm{d}\theta\,\mathrm{d}z$$
$$\bar{D}(r,t) = \frac{1}{2\pi}\int_0^t \int_0^{2\pi} \phi(r,\theta,0,t)\,u_s \mathrm{d}\theta\,\mathrm{d}t \qquad (7)$$

Initially, the areal deposition along the lock length ($0 \leq r \leq R_0$) increases linearly with time up to the point where all the fluid inside the lock has been set in motion ($t \approx 6$). The current is shown to attain the typical slug like shape with a relatively thick head and a slender body around $t = 4$. At $t = 10$, the areal deposition profile begins to converge towards its final form with two local maxima becoming identifiable with the largest of the two developing at close proximity to the gate at a radial distance of $r = 2$, and the smaller of the two appearing farther downstream around $r = 3.5$. As seen from Fig. 6, the effect of sedimentation on the spreading rate of the current is not perceived until enough particles have settled out. This occurs sometime between $t = 10$ and $t = 16$, where the particle-laden current front begins to deviate from the saline current. During that time frame, the current has lost over 45 percent of its total particles (see Fig. 7).

3.3. Front location

The front position of the current is shown in Fig. 6. Because of the axisymmetric nature of spreading, the concentration field is first averaged in the azimuthal direction. The position of the front (r_N) is then taken as the location where the vertically averaged concentration (the current's thickness) drops to a value of 0.01. Our numerical domain was chosen to match the physical setting of experiments reported by Bonnecaze et al. [3], and their findings are plotted alongside our simulation data in Fig. 6. Our results for the larger and smaller *Re* number simulations are in good agreement with the experiments and the Shallow Water equations-based theoretical model. The larger *Re* number case of 10,000, which is closer to the *Re* of the experiments of 17,000, provides however, slightly better agreement with the experiments and SW model. In addition to the particle-laden currents, we also show the front location for a saline current experiment carried out by Bonnecaze et al. [3]. The saline current experiment serves as a benchmark to identify the time beyond which sedimentation effects influence the front velocity of the particle-laden current.

The aforementioned experiments were carried out in a radial sector tank with monodisperse 37 μm silicon carbide particles resulting in a non-dimensional settling velocity of 1.3×10^{-2}. This is precisely the non-dimensional settling velocity used in the present simulations. The initial reduced gravitational acceleration for the particle-laden and saline currents were 11 cm s^{-2} and 42 cm s^{-2}, respectively.

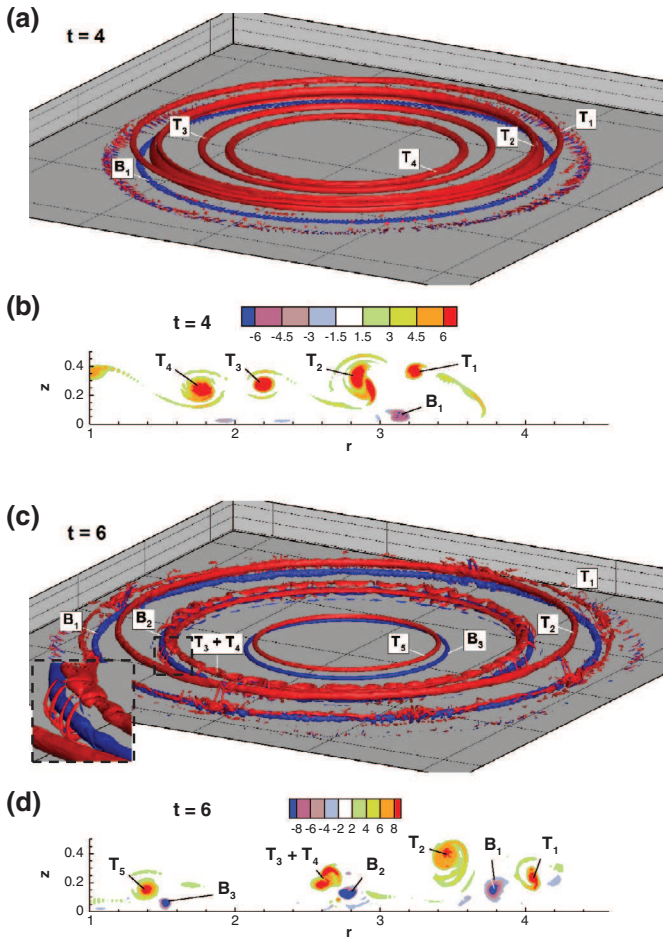

Fig. 4. (a) and (c) iso-surfaces of λ_{ci} (multiplied by the sign of the azimuthal vorticity $|\omega_\theta|/\omega_\theta$) for $Re = 10000$ with isovalues of 6 and 8 for $t = 4$, and $t = 6$, respectively. A close-up view at $t = 6$ shows a set of inclined hairpin vortical structures that have formed around the bottom clockwise rotating vortex B_2 in the body of the current. The blue (resp. red) color indicates clockwise (resp. counter-clockwise) rotation. (b) and (d) contours of λ_{ci} (multiplied by the sign of the azimuthal vorticity $|\omega_\theta|/\omega_\theta$) in the vertical $y = 0$ plane for $t = 4$, and $t = 6$, respectively. (For interpretation of the references to color in this figure legend, the reader is referred to the web version of this article).

Despite the difference in the reduced gravitational acceleration, the non-dimensional front positions of these currents perfectly match until enough particles have settled out and the two curves begin to diverge from one another.

3.4. Deposition

Of fundamental importance in particle-laden gravity currents is the deposition pattern of sediments. The settling of particles leads to a continuous decrease in the density of the current leading to a decay in the driving force, and eventually causing the current to arrive at a standstill when all the particles have settled out. The total deposited mass (normalized by the initial mass in the domain), M, is shown in Fig. 7 for the $Re = 3450$ and $Re = 10000$ cases. Here, M is computed as

$$M(t) = \frac{\int_0^{L_y}\int_0^{L_x}\int_0^{t}\phi(x,y,0,t)u_s\,dt\,dx\,dy}{\int_0^{L_y}\int_0^{L_x}\int_0^{H}\phi(x,y,z,0)\,dz\,dx\,dy}. \tag{8}$$

Both curves are in good agreement up to $t \approx 10$ at which point the total mass deposited from the $Re = 10000$ case becomes larger than that corresponding to the $Re = 3450$ case. This is somewhat counter-intuitive as one would expect enhancement of turbulence to better mix (destratify the concentration profile) and thus hinder the deposition process. However, there are other factors that could affect the deposition rate in the simulations. The horizontal extent of the current could be such a factor. The wider the surface the current covers, the larger the area overwhich the current can deposit particles. From Fig. 6, we observe the current for the $Re = 10000$ case to advance faster and cover more distance than for the $Re = 3450$ case. In particular at $t = 30$, the run out distance for the $Re = 10000$ (resp. $Re = 3450$) case is 9.1 (resp. 8.6). This results in an area increase of 12%, and provides a possible explanation to the enhanced deposition for the larger Re case. In the inset of Fig. 7, we show the total deposited mass M further normalized by the horizontal area of the current, πr_N^2, and then multiplied by 1000. Here we observe that the lower Re case beyond $t \approx 8$ to deposit more sediments per unit area of the current. As mentioned earlier, the lower the Reynolds number, the more stratified the vertical concentration profile, and the larger the deposit per unit area of the current.

Fig. 8 illustrates the temporal evolution of the rate of deposition of suspended particles defined as

$$\dot{m}(t) = \int_0^{L_y}\int_0^{L_x}\phi(x,y,0,t)u_s\,dx\,dy \tag{9}$$

We observe a rise in the sedimentation rate from the time of release up to $t = 8$, beyond which the particles continue to settle but at a continuously diminishing rate. Immediately after release, the current begins to deposit particles over a circular surface of radius R_0. However, as the current starts to spread radially outward, its surface area increases with the bottom concentration remaining at a relatively high level leading to a rise in the sedimentation rate as observed in Fig. 8 ($0 < t < 8$). At a certain instant however ($t \approx 8$), the bottom concentration has become dilute enough, that the deposition rate begins to decline despite its continuously increasing front position. This behavior of rise and decay in the sedimentation rate has been also observed for planar particle-driven gravity currents [18].

The local instantaneous deposition rate is strongly affected by the large-scale vortex tubes shown in Fig. 4. These tubes create local minima in the instantaneous bottom concentration profile (and hence the instantaneous deposition rate) by transporting low concentration fluid (particle-laden current mixed with the ambient) towards the bottom wall. Consider for instance the 2-dimensional concentration profile on the bottom wall at $t = 6$ as shown in Fig. 9. We may readily identify a local minimum at $r \approx 2.5$, where the bottom concentration drops by about 14%. The position of this minimum corresponds to the radial location of the vortex tube labeled $T_3 + T_4$. Except for the aforementioned drop in the bottom concentration at $r \approx 2.5$, the current appears to deposit its sediments uniformly in the domain $1 < r < 3.5$. At $r \approx 4$ however, the three-dimensionality of the flow is strong due to the effect of the lobe and cleft instability at the front as well as the inclined hairpin vortices that emerge from the bottom wall around the front of the current as seen in Fig. 4.

For the sake of comparison with experiments, we plot in Fig. 10 the areal deposition from both simulations and compare them with Bonnecaze et al. [3] experimental and theoretical final deposition layout. The areal density of deposit of the simulations is taken at $t = 30$, at which point over 95% (resp. 91%) of particles have settled for the $Re = 10000$ (resp. $Re = 3450$) case.

The simulation curves are scaled so that the area under the curve is equivalent to that of the experimental results. The simulations as well as the theoretical model indicate that the current's density of deposit increases as we move away from the center and reaches a maximum value close to ($r = 2$). This is in contrast with the experiments where the density of deposit decreases monotonically as we move radially outwards. Differences between simulation and experiments are most distinct in the region around the lock. However, for the experiments, the region behind the gate is subject to disturbances

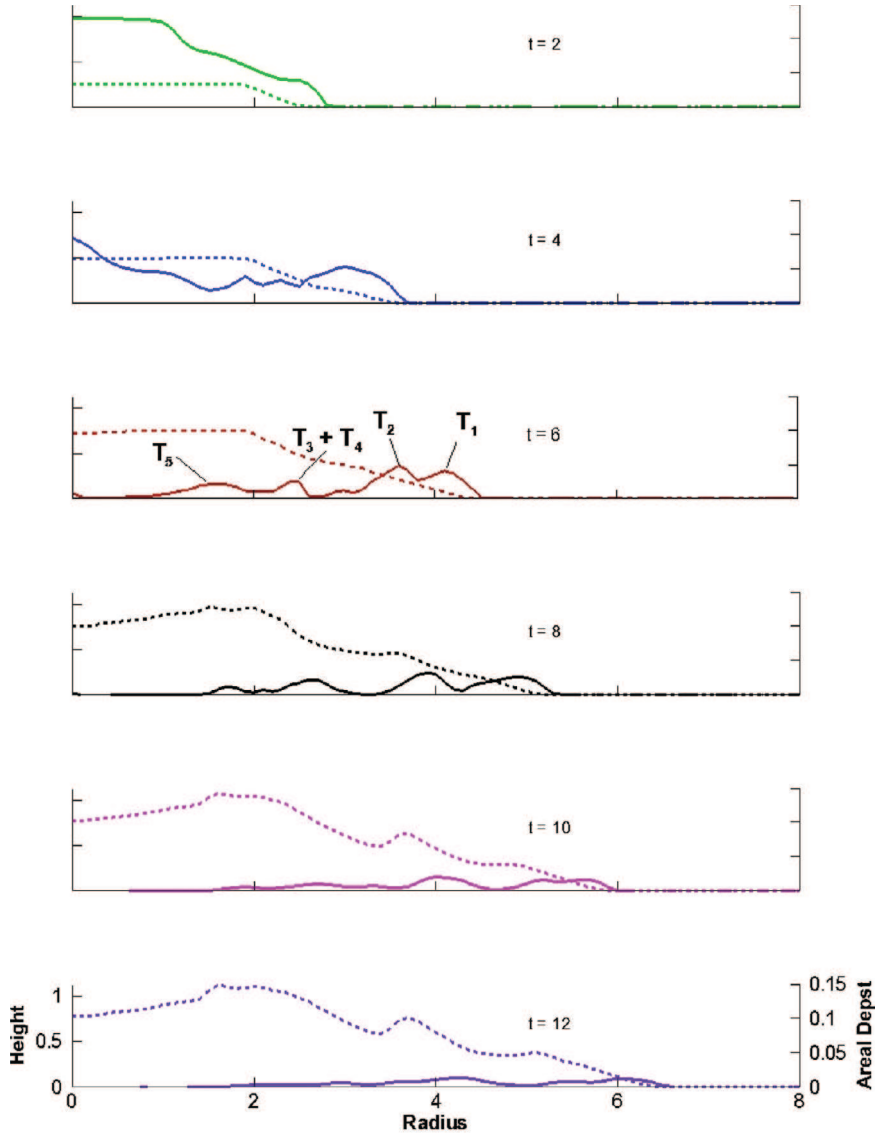

Fig. 5. Height (solid line) and areal deposit (dashed line) as a function of radius for different times with $Re = 10000$. The four peaks in the height profile at $t = 6$ correspond to the Kelvin–Helmholtz vortices shown in Fig. 3. The Kelvin–Helmholtz vortices at $t = 4$ are not as readily identifiable, perhaps because of the relatively smaller radial variations in the density profile.

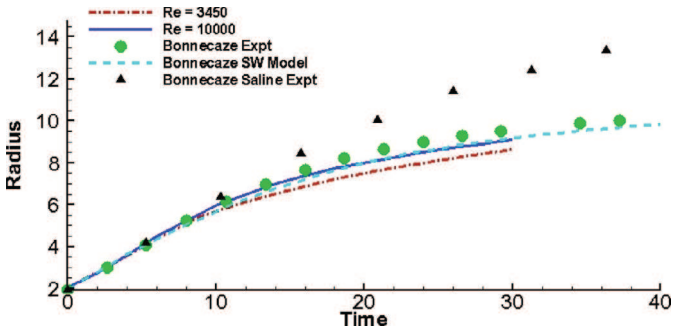

Fig. 6. Evolution of the front as a function of time. The solid and dash-dotted lines are from the present simulation. The circular and triangular symbols are from Bonnecaze et al. [3] experiments for particle-laden currents with 37 μm-diameter silicon carbide particles with an initial reduced gravity of $g_0' = 11$ cm s^{-2}-, and a saline current with $g_0' = 42$ cm s^{-2}, respectively. The dashed line is the solution of a theoretical model based on the Shallow Water equations from Bonnecaze et al. [3].

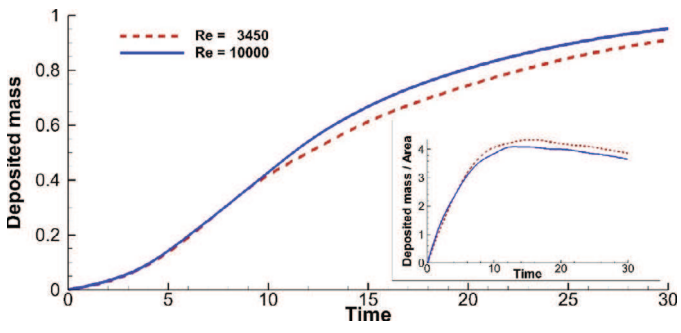

Fig. 7. Total mass of settled particles as a function of time for$Re = 3450$ and $Re = 10000$. Results are normalized with the initial mass of suspended particles. (Inset) Same as main figure, but results are further normalized by the horizontal area of the current and multiplied by 1000.

from initial stirring in addition to the early sedimentation that initiates before the removal of the gate. The DNS results in Fig. 10, also reveal a second peak in the amount of deposition at a downstream location from the gate. It should be noted however that the amplitude of these peaks is observed to decrease with increasing Reynolds number. The presence of multiple spikes have also been observed in planar simulations of particle-laden currents [18].

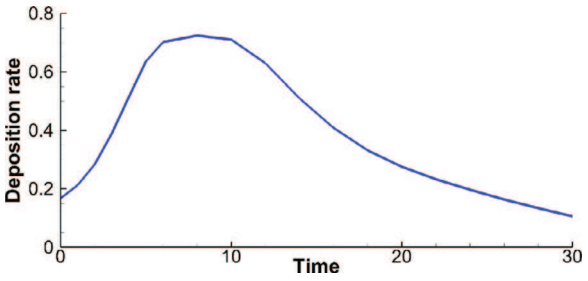

Fig. 8. Deposition rate versus time at the bottom wall of the domain for $Re = 10000$. The sedimentation rate increases from the time of release, attains a maximum value around $t = 8$, then monotonically diminishes up to the end of the simulation.

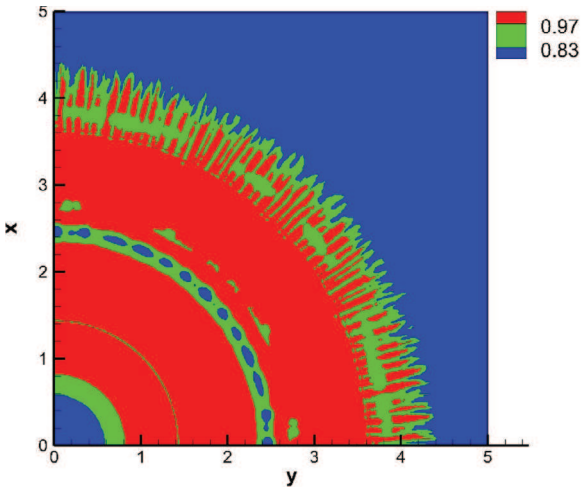

Fig. 9. Contours of concentration at the bottom wall for $Re = 10000$ in one quadrant of the computational domain at $t = 6$. The large scale vortex tubes transport low concentration fluid (particle-laden fluid mixed with the ambient) from the top of the current towards the bottom wall resulting in a local minimum around the radial distance $r = 2.5$.

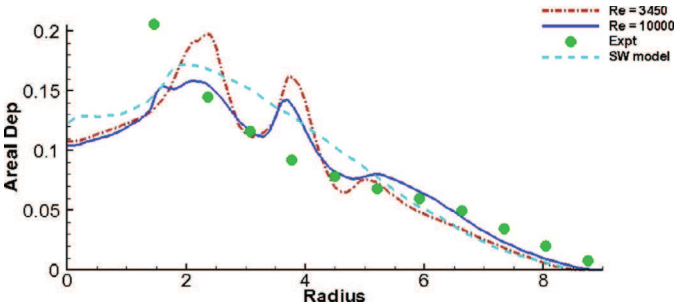

Fig. 10. Final areal density of deposit from simulation, experiment, and theoretical model. The experiments and theoretical model results are extracted from Bonnecaze et al. [3].

3.5. Wall shear-stress and near-wall dynamics

Exploring the near-wall dynamics of a particulate gravity current is necessary for understanding erosion and resuspension of particles. The wall-shear stress is often used in theoretical models to predict the possibility of sediment entrainment over loose beds [25,27,19]. The dimensional wall-shear stress in the radial direction is defined as

$$\tau_w = \mu \left. \frac{\partial u_R^*}{\partial z^*} \right|_{z^*=0} \tag{10}$$

where, μ represents the dynamic viscosity of the current, u_R^* is the dimensional horizontal component of velocity in the radial direction,

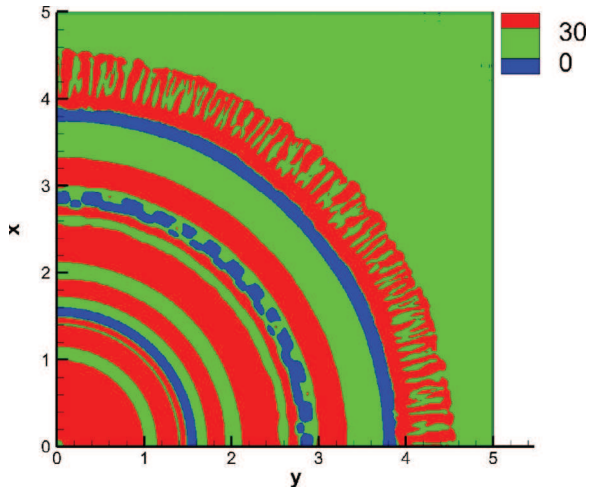

Fig. 11. Contours of the radial bottom shear stress for $Re = 10000$ in one quadrant of the computational domain at $t = 6$. The wall shear stress is strongly affected by the clockwise-rotating bottom vortex tubes shown in Fig. 4. Here, the wall-shear stress is multiplied by $Re/(\rho_{c0}^* U^2)$, where ρ_{c0}^* is the dimensional initial density of the current.

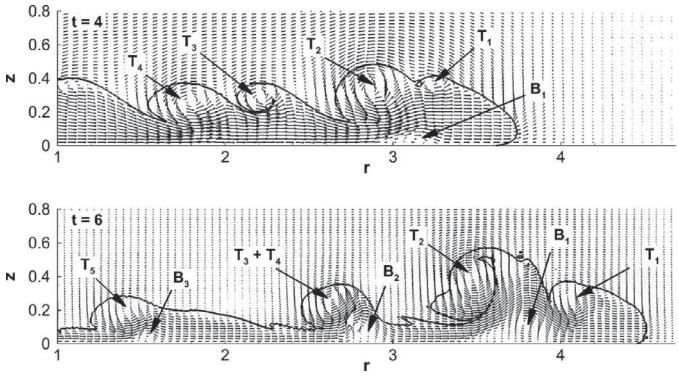

Fig. 12. In-plane velocity field in the vertical, $y = 0$, plane at $t = 4$ and $t = 6$ for $Re = 10000$ case. The current layout is visualized by a concentration contour of $\phi = 0.05$. The top (resp. bottom) vortices rotate with a counter-clockwise (resp. clockwise) direction.

and $z^* = z \times H$ is the dimensional vertical coordinate ($z^* = 0$ signifying the location of the bottom plane).

These bed-shear stresses are closely related to the large scale clockwise rotating vortex tubes discussed in Section 3.1. A two-dimensional contour plot in Fig. 11 of the wall shear-stress at $t = 6$ reveals three local minima with a local region of reversal in flow direction (negative wall shear-stress). These local minima correspond to the clockwise rotating vortex tubes sweeping the bottom wall (B_1, B_2, and B_3). The vortex tubes $B_1$and B_3 are relatively smooth with small variations along the radial direction. Their axisymmetric structure is translated into a smooth shell-like outline in the wall shear-stress contours of Fig. 11. On the other hand, the hairpin and other small-scale vortical structures forming around B_2 (see Fig. 4) is the reason behind the wavelike pattern at $r \approx 2.8$ in Fig. 11. The local minima in the bottom shear-stress profile of Fig. 11 are a result of flow reversal due to the aforementioned clockwise vortex tubes rotating at close proximity to the bottom wall. The direction of these vortices and their position with respect to the current is presented in Fig. 12. Here, a vertical two-dimensional section of the domain ($y = 0$ plane) shows the in-plane velocity field along with the position of the current visualized by a contour of $\phi = 0.05$. The current is observed to take a slug-like shape constituting of a head and a body, where the head extends from the front of the current ($r \approx 4.5$) until the location

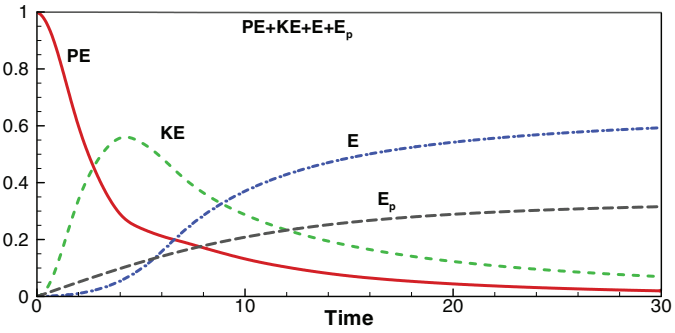

Fig. 13. Temporal evolution of the potential energy (PE), kinetic energy (KE), and dissipation (E and E_p), defined in (11) and (16), respectively, of the $Re = 10000$ turbidity current. The sum of all four terms is shown as the thin black line.

of the top vortex T_1, ($r \approx 4$). The body is seen to have multiple undulations mostly caused by the top counter-clockwise rotating vortices.

3.6. Energy budget

The potential to kinetic energy transformation is of fundamental interest in the study of gravity currents. In the present setup, the total potential (PE) and kinetic (KE) energies are defined as

$$\mathrm{PE}(t) = \int_0^H \int_0^{L_y} \int_0^{L_x} \phi\, z\, dxdydz$$
$$\mathrm{KE}(t) = \frac{1}{2} \int_0^H \int_0^{L_y} \int_0^{L_x} \mathbf{u}^2\, dxdydz. \tag{11}$$

Initially, all the energy in the domain is in the form of potential energy, however as the current begins to spread, part of this potential energy is used to set the flow in motion, while part is lost to viscous dissipation. There are two types of dissipation for particle-laden currents. The first, denoted here as σ, is a result of the gradient of the meso-scale velocity field, it is defined as

$$\sigma(t) = \frac{2}{Re} \int_0^H \int_0^{L_y} \int_0^{L_x} \boldsymbol{\varepsilon} \cdot \boldsymbol{\varepsilon}\, dxdydz, \tag{12}$$

where ε is the strain-rate tensor of the computed meso-scale velocity field. The second type of dissipation is at the micro-scale and is caused by the Stokes flow around the individual particles [10]. Even though our numerical model does not resolve the flow around the individual particles, the latter dissipation may be computed from the local concentration field, viz

$$\sigma_p(t) = -\int_0^H \int_0^{L_y} \int_0^{L_x} \left(\frac{1}{ScRe} z\nabla^2\phi + z\, u_s \frac{\partial \phi}{\partial z} \right) dxdydz. \tag{13}$$

The global energy budget, which is derived from the momentum and transport Equations (2) and (4), respectively, may be expressed as

$$\frac{D}{Dt}(PE + KE) + \sigma + \sigma_p = 0, \tag{14}$$

Integrating (14) with respect to time, we obtain

$$PE + KE + \mathrm{E} + \mathrm{E}_p = \mathrm{PE}_0, \tag{15}$$

where

$$\mathrm{E} = \int_0^t \sigma(\eta)\, d\eta, \quad \mathrm{E}_p = \int_0^t \sigma_p(\eta)\, d\eta, \tag{16}$$

and $\mathrm{PE}_0 = \mathrm{PE}(t = 0)$ is the total initial potential energy in the domain. Fig. 13 shows the temporal evolution of the four terms on the left hand side of (15) normalized by PE_0. During the early stages of the release (up to $t = 4$), there is a fast conversion of potential to kinetic energy, as the current loses around 70% of its initial potential energy. This fast decline in the available potential energy is accompanied by a rapid increase in kinetic energy. Beyond that time, the potential energy in the system continues to drop due to the finite nature of the release (no external source of energy), whereas the kinetic energy is observed to reach a maximum value ($KE \approx 0.56PE_0$) around $t = 5$ before starting to decay as a result of viscous dissipation, in the present case of cylindrical release for which $Re = 10000$ and $u_p = 0.013$. The dissipation is mostly dominated by E_p in the early stages of the flow (up to$t \approx 5$), however as more particles settle out towards the bottom wall, the macroscopic dissipation term E becomes the dominant dissipation term being almost twice as large as that due to sedimentation at larger times, say $t > 20$. Note that in the case of a planar release with $Re = 2236$ and $u_p = 0.02$, Necker et al. [18] found a similar evolution of the kinetic energy and dissipation, as in their case the maximum value of KE was $0.52PE_0$ at $t = 3$ and $\mathrm{E} = 1.5\mathrm{E}_p$ for $t > 20$, approximately. The lower value of E relative to E_p in their case may be attributed to the larger value of the settling velocity ($u_p = 0.02$ vs 0.013 in our case) which is likely to increase the contribution of dissipation due to sedimentation.

4. Conclusions

We present direct numerical simulation results for a cylindrical, finite-release, particle-laden gravity current. At early times ($t < 6$), the current shows a train of Kelvin–Helmholtz counter-clockwise rotating rolled up tubes that are generated along the current–ambient interface. Below these vortex tubes, a set of clockwise-rotating eddies initiate from the bottom wall. These large scale vortical structures are difficult to visualize and study experimentally and are unattainable using depth-averaged, two-dimensional theoretical models. They are nonetheless very important for studying the erosion, deposition, and resuspension dynamics of particle-laden currents. These vortex tubes may locally modify the bed shear stress and hence could play an important role in particle entrainment and erosion off the bottom wall. Furthermore, by transporting low particle concentration fluid from the surface of the current towards the bottom wall, they locally change the bottom concentration and hence modify the deposition pattern as well. Our simulations compare favorably with previous experiments [3] in terms of the temporal evolution of the front as well as the final deposition pattern.

Acknowledgments

This study was supported by the Chateaubriand Fellowship provided by the French Embassy in the USA as well as the National Science Foundation Partnership for International Research and Education (PIRE) grant (NSF OISE-0968313). The two anonymous reviewers are thanked for their detailed and insightful comments which greatly improved the quality of the paper.

References

[1] Blanchette F, Strauss M, Meiburg E, Kneller B, Glinsky M. High-resolution numerical simulations of resuspending gravity currents: condition for self-sustainment. J Geophys Res 2005;110:c12022.
[2] Bonnecaze R, Huppert H, Lister J. Particle-driven gravity currents. J Fluid Mech 1993;250:339–69.
[3] Bonnecaze R, Hallworth M, Huppert H, Lister J. Axisymmetric particle-driven gravity currents. J Fluid Mech 1995;294:93–122.
[4] Cantero M, Lee JR, Balachandar S, Garcia M. On the front velocity of gravity currents. J Fluid Mech 2007;586:1–39.
[5] Cantero M, Balachandar S, Garcia M. High-resolution simulations of cylindrical density currents. J Fluid Mech 2007;590:437–69.
[6] Cantero M, Balachandar S, García M. An Eulerian–Eulerian model for gravity currents driven by inertial particles. Int J Multiphase Flow 2008;34:484–501.
[7] Chakraborty P, Balachandar S, Adrian R. On the relationships between local vortex identification schemes. J Fluid Mech 2005;535:189–214.
[8] Choi S-U, Garcia M. Modeling of one-dimensional turbidity currents with a dissipative-Galerkin finite element method. J Hydra Res 1995;33(5):623–48.
[9] Dade W, Huppert H. A box model for non-entraining suspension-driven gravity surges on horizontal surfaces. Sedimentology 1995;42:453–71.

[10] Espath LFR, Pinto LC, Laizet S, Silvestrini JH. Two-and three-dimensional direct numerical simulation of particle-laden gravity currents. Comput Geosci 2014;63:9–16.
[11] Garcia M, Parker G. Experiments on the entrainment of sediment into suspension by a dense bottom current. J Geophys Res 1993;98(C3):4793–807.
[12] Gladstone C, Phillips JC, Sparks RSJ. Experiments on bidisperse, constant-volume gravity currents: propagation and sediment deposition. Sedimentology 1998;45:833–44.
[13] Gladstone C, Woods A. On the application of box models to particle-driven gravity currents. J Fluid Mech 2000;416:187–95.
[14] Hallworth M, Huppert H. Abrupt transitions in high-concentration, particle-driven gravity currents. Phys Fluids 1998;10:1083.
[15] Härtel C, Carlsson F, Thunblom M. Analysis and direct numerical simulation of the flow at a gravity-current head. Part 2. The lobe-and-cleft instability.. J Fluid Mech 2000;418:213–29.
[16] Hogg A, Hallworth M, Huppert H. On gravity currents driven by constant fluxes of saline and particle-laden fluid in the presence of a uniform flow. J Fluid Mech 2005;539:349–85.
[17] Lowe DR. Sediment gravity flows: II Depositional models with special reference to the deposits of high-density turbidity currents. J Sed Res 1982;52.
[18] Necker F, H¨artel C, Kleiser L, Meiburg E. High-resolution simulations of particle-driven gravity currents. Intl J Multiphase Flow 2002;28:279–300.
[19] Parker G, Fukushima Y, Pantin HM. Self accelerating turbidity currents. J Fluid Mech 1986;171:145–81.
[20] Shringarpure M, Cantero M, Balachandar S. Dynamics of complete turbulence suppression in turbidity currents driven by monodisperse suspensions of sediment. J Fluid Mech 2012;712:384–417.
[21] Simpson JE. Effects of the lower boundary on the head of a gravity current. J Fluid Mech 1972;53:759–68.
[22] Simpson JE. Gravity currents in the laboratory, atmosphere, and ocean. Ann Rev Fluid Mech 1982;14:213–34.
[23] Sequeiros O, Naruse H, Endo N, Garcia M, Parker G. Experimental study on self-accelerating turbidity currents. J Geophys Res 2009;114:C05025.
[24] Ungarish M, Huppert H. The effects of rotation on axisymmetric gravity currents. J Fluid Mech 1998;362:17–51.
[25] Yalin MS, Karahan E. Inception of sediment transport. J Hydraul Div 1979;105(11):1433–43.
[26] Ziskind G, Fichman M, Gutfinger C. Resuspension of particulates from surfaces to turbulent flows – review and analysis. J Aerosol Sci 1995;26:613–44.
[27] Zeng J, Lowe DR. Numerical simulation of turbidity current flow and sedimentation: I. Theory.. Sedimentology 1997;44(1):67–84.
[28] Zhou J, Adrian R, Balachandar S, Kendall T. Mechanics for generating coherent packets of hairpin vortices. J Fluid Mech 1999;387:353–96.